

See discussions, stats, and author profiles for this publication at: <https://www.researchgate.net/publication/279988634>

# Large-Area Nanoimprinted Colloidal Au Nanocrystal-Based Nanoantennas for Ultrathin Polarizing Plasmonic Metasurfaces

ARTICLE in NANO LETTERS · JULY 2015

Impact Factor: 13.59 · DOI: 10.1021/acs.nanolett.5b02647 · Source: PubMed

---

READS

86

9 AUTHORS, INCLUDING:



**Mykhailo Tymchenko**

University of Texas at Austin

16 PUBLICATIONS 73 CITATIONS

SEE PROFILE



**Xingchen Ye**

University of California, Berkeley

57 PUBLICATIONS 2,773 CITATIONS

SEE PROFILE



**Christopher B Murray**

University of Pennsylvania

260 PUBLICATIONS 27,653 CITATIONS

SEE PROFILE



**Cherie R Kagan**

University of Pennsylvania

105 PUBLICATIONS 9,145 CITATIONS

SEE PROFILE

# Large-Area Nanoimprinted Colloidal Au Nanocrystal-Based Nanoantennas for Ultrathin Polarizing Plasmonic Metasurfaces

Wenxiang Chen,<sup>†</sup> Mykhailo Tymchenko,<sup>||</sup> Prashanth Gopalan,<sup>‡</sup> Xingchen Ye,<sup>§</sup> Yaoting Wu,<sup>§</sup> Mingliang Zhang,<sup>‡</sup> Christopher B. Murray,<sup>‡,§</sup> Andrea Alu,<sup>||</sup> and Cherie R. Kagan<sup>\*,†,‡,§</sup>

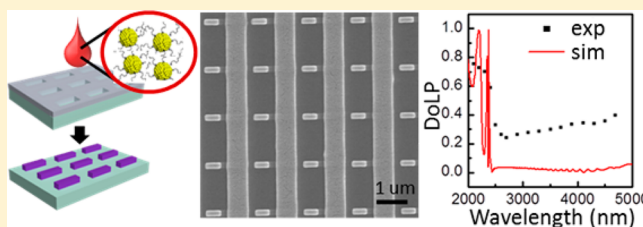
<sup>†</sup>Department of Electrical and Systems Engineering, <sup>‡</sup>Department of Materials Science and Engineering, and <sup>§</sup>Department of Chemistry, University of Pennsylvania, Philadelphia, Pennsylvania 19104, United States

<sup>||</sup>Department of Electrical and Computer Engineering, The University of Texas at Austin, Austin, Texas 78712, United States

## S Supporting Information

**ABSTRACT:** We report a low-cost, large-area fabrication process using solution-based nanoimprinting and compact ligand exchange of colloidal Au nanocrystals to define anisotropic, subwavelength, plasmonic nanoinclusions for optical metasurfaces. Rod-shaped, Au nanocrystal-based nanoantennas possess strong, localized, plasmonic resonances able to control polarization. We fabricate metasurfaces from rod-shaped nanoantennas tailored in size and spacing to demonstrate Au nanocrystal-based quarter-wave plates that operate with extreme bandwidths and provide high polarization conversion efficiencies in the near-to-mid infrared.

**KEYWORDS:** Plasmonics, nanocrystals, nanoimprinting, optical nanoantennas, metasurface, waveplate



Optical metamaterials are constructed from arrangements of subwavelength, plasmonic building blocks that are tailored in size and shape.<sup>1–3</sup> While three-dimensional metamaterials have been shown to manipulate light propagation in the bulk, with exotic effects in both the near and far fields, two-dimensional metasurfaces have recently drawn a lot of attention as alternatives for their simpler design and fabrication, and for their comparable ability to enhance electromagnetic fields and control light polarization. Metasurfaces consisting of subwavelength plasmonic inclusions arranged in two-dimensional arrays have been demonstrated to manipulate visible and infrared absorption,<sup>4–7</sup> luminescence,<sup>8–10</sup> and scattering<sup>6,11,12</sup> in a variety of devices, such as sensors,<sup>7,13,14</sup> photodetectors and photovoltaics,<sup>15–17</sup> flat plasmonic metalenses,<sup>18–20</sup> quarter-wave plates,<sup>21–24</sup> optical resonator interfaces,<sup>25,26</sup> and holography plates.<sup>27,28</sup> However, to define the nanoscale size, complex shapes, and intricate spatial arrangement of plasmonic building blocks in most two-dimensional metasurfaces, they have generally been fabricated by electron-beam lithography with subsequent metal evaporation or by focused-ion beam lithography to ion mill deposited thin metal films. These methods are expensive and time-consuming, because they require many consecutive steps and the use of high vacuum during metal deposition, which hinders large-area fabrication.

Nanoimprint lithography provides a low-cost, large-area, high-throughput alternative technique for patterning the subwavelength structures constituting optical metasurfaces.<sup>29–32</sup> Colloidal metal nanocrystals (NCs) behave like inks that allow solution-based deposition of metal nanostructures over large areas, promising to drive down the cost of

production.<sup>33–35</sup> In recent reports, direct nanoimprint lithography of templates into Au NC dispersions deposited on substrates were shown to produce arrays of subwavelength, plasmonic nanopillars of simple shape.<sup>33,36</sup> However, these simple Au NC-based nanopillar arrays were large in size and/or pitch, had significant nonuniformities in edge roughness and shape, and were of limited thickness. Most metasurface devices require more complex, anisotropic plasmonic inclusions that are uniform in shape, tailored in height, and closely spaced to locally control the intensity, the phase, and the polarization of transmitted light,<sup>7,8,18–23,25–28,37</sup> than those accessible by direct nanoimprinting. Here we demonstrate that thermal nanoimprint lithography and solution-based deposition of colloidal Au NCs can be successfully combined to fabricate metasurfaces consisting of plasmonic nanorods of various size, shape, and spacing. By engineering the dimensions of the nanorods, we are able to tune the frequency of their plasmonic resonance and the magnitude and phase of their polarization.

We exploit nanoimprinting of NC-based nanorods to demonstrate the first NC-based optical devices. We select to design and build ultrathin quarter-wave plates (QWPs) from the orthogonal arrangement of different size nanorods. The orthogonal arrangement of nanorods introduces the 90° phase difference between two orthogonal, linearly polarized components of transmitted light, required for QWP operation. By changing the size and distance between orthogonal nanorods, we tailor the phase difference and the amplitude of transmitted

Received: April 20, 2015

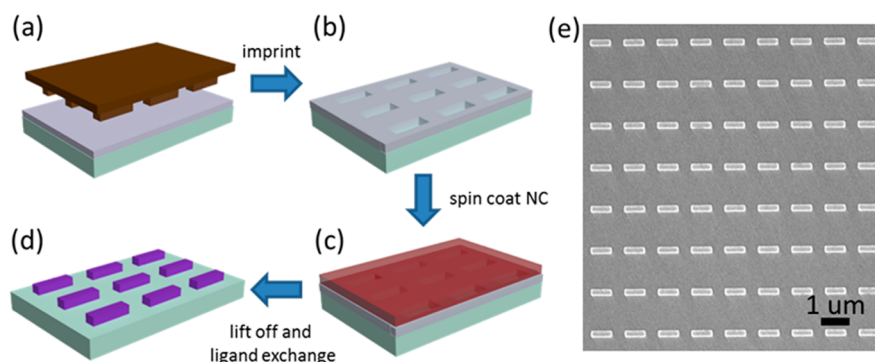


**Figure 1.** Nanoantenna fabrication by (a) thermal nanoimprint lithography to (b) transfer the master pattern into the resist, followed by (c) spin-coating of colloidal Au NCs and (d) ligand exchange and resist lift-off. (e) SEM image of a representative NC-based nanoantenna array fabricated by the nanoimprinting method.

linearly polarized waves.<sup>21,38</sup> We construct two different large-area, ultrathin NC-based QWPs to emphasize the ease and flexibility of this approach and to customize the frequency and bandwidth of operation, notably experimentally demonstrating the first extreme bandwidth QWP.

We synthesize 5 nm diameter oleylamine (OAm)-capped colloidal Au NCs, following previously published methods.<sup>12,39</sup> These NCs are patterned into anisotropic, subwavelength, NC-based nanostructure arrays by nanoimprint lithography. Master templates patterned with nanorod arrays are defined by electron-beam lithography and are then used repeatedly in the subsequent nanoimprint process. Supporting Information Figure S1 shows an example of a master template patterned with 816 nm × 242 nm nanorods. Figure 1a–d shows the schematic of the process used to make Au NC-based plasmonic nanorod arrays. First, thermal nanoimprint lithography (Figure 1a,b) is used to transfer the nanostructure pattern of the master template into the thermal imprint resist. Au NC dispersions in hexane are then deposited by spin-coating (Figure 1c). The thermal imprint resist is lifted off by placing samples in an acetone bath for 10 s with mild shaking or sonication, leaving the nanorods atop the substrate. Finally, the samples are immersed in 8 mg/mL solutions of NH<sub>4</sub>SCN in acetone to chemically exchange the long OAm ligands used in synthesis for the more compact thiocyanate (SCN) (Figure 1d). Our group has shown previously that compact ligand exchange increases the coupling between Au NCs, inducing an insulator-to-metal transition in Au NC thin films.<sup>33</sup>

Figure 1e shows a representative scanning electron micrograph (SEM) of a Au NC-based nanorod array. SEM images are taken from different regions of the sample to determine the uniformity in the nanorod dimensions across the array (Supporting Information, Figure S2). Across the 1.44 mm<sup>2</sup> sample area, the size and size variation in the nanoantenna length is 749 nm ± 13 nm, and the width is 229 nm ± 5 nm. The line edge roughness (LER) for the NC-based nanoantennas is 2.9 nm, and the misalignment, defined as the standard deviation in the orientation of the nanorods, is 0.4° (Supporting Information, Table 1). The dimensions of the imprinted nanoantennas are 5–20% smaller than the features in the master template due to shrinkage of the NC-based nanostructures as the long OAm ligands used to synthesize and disperse the Au NCs in solution are replaced by the compact SCN ligands. The degree of shrinkage depends on the amount of OAm ligands in the NC dispersion and may be reduced by removing excess ligands by washing, but not too

much such that the NC dispersion becomes unstable and unusable. We note that the LER and misalignment of the nanoimprinted nanoantennas are similar to that for a Au NC nanorod array patterned by e-beam lithography (Supporting Information, Figure S3 and Table 1).

We also investigate the uniformity in nanorod height. Nanoantenna arrays with heights ranging from 71 to 119 nm are fabricated by controlling the concentration of the Au NC dispersions used in spin-coating from 10 mg/mL to 20 mg/mL. Variations in height across the nanorods are evident by the contrast in atomic force microscopy images and by the line cuts shown in Supporting Information, Figure S4a–d. The nanorods are taller at their edges akin to a “rabbit ear” effect that may arise from (1) incomplete filling of the Au NCs, (2) greater adhesion between the Au NCs and the resist layer, and/or (3) lift-off.<sup>40,41</sup> The height difference between the nanorod edge and the nanorod center is reduced for the thicker 119 nm NC films (Supporting Information, Figure S4d), allowing the fabrication of more uniform nanorods. As the height of the nanoantenna arrays increases, the plasmon resonance extinction increases and blue shifts (Supporting Information, Figure S4e). The increased extinction is caused by the larger amount of plasmonic material in each nanorod. The increased height also weakens the hybridization of the surface plasmons located at the top and bottom surfaces of the nanorod, leading to a blue shift in the resonance,<sup>42</sup> a counterintuitive effect for nanostructures, since it leads to a blue shift despite the increase in volume.<sup>43</sup> It is worth noting that the resonance shift is nonlinear. For thinner films approaching the 30 nm skin depth of Au, the shift becomes much more significant than that for the thicker films studied here.<sup>31</sup>

Using nanoimprint lithography we fabricate arrays of nanorods tailored in size to have lengths and widths of (a) 863 nm × 167 nm, (b) 680 nm × 178 nm, (c) 470 nm × 200 nm, and (d) 178 nm × 178 nm (Figure 2a–d). Their horizontal (0 degree direction in the inset in Figure 2a) and vertical (90° direction) pitches are (a) 1.5 μm × 1.5 μm, (b) 1.2 μm × 1.5 μm, (c) 0.9 μm × 1.5 μm, and (d) 0.63 μm × 0.63 μm. As the pitches are different among these four samples, in the following transmittance spectra, we normalize the magnitude of the transmittance to the density of nanorods.

The nanoantenna length is a major factor in controlling its dipole plasmonic resonance. We apply finite-difference frequency-domain simulations to predict the transmittance spectra for these four samples (Figure 2e, upper panel). The dielectric function of SCN-exchanged Au NC thin films is

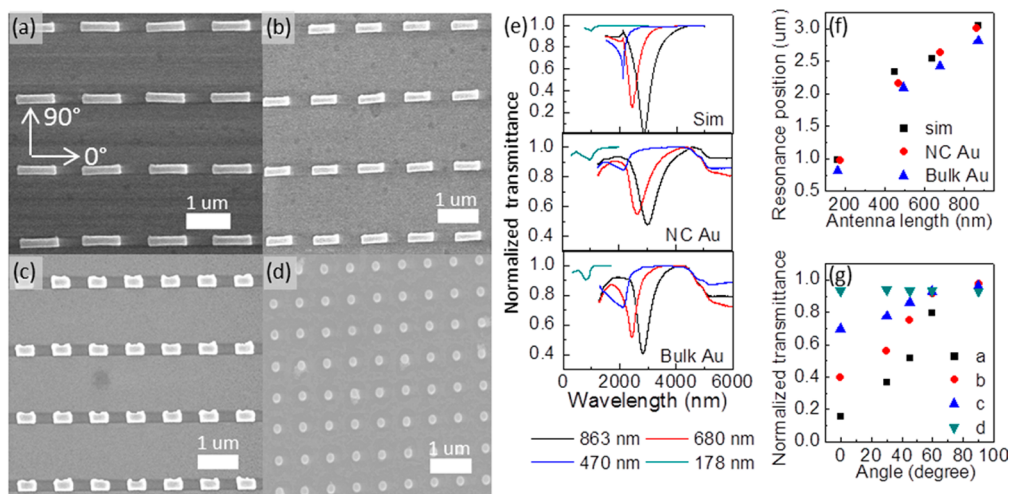


**Figure 2.** SEM images of Au NC-based nanoantenna arrays with length  $\times$  width of (a) 863 nm  $\times$  167 nm, (b) 680 nm  $\times$  178 nm, (c) 470 nm  $\times$  200 nm, and (d) 178 nm  $\times$  178 nm. (e) Normalized transmittance spectra for these Au NC-based nanoantenna arrays from (upper panel) finite difference frequency-domain simulations and (middle panel) FT-IR measurements. Black, red, blue, and green curves correspond to the nanoantenna arrays shown in a–d. (bottom panel) Comparison to the transmittance spectra for bulk Au nanoantenna arrays of similar sizes: (black) 868 nm  $\times$  188 nm, (red) 677 nm  $\times$  228 nm, (blue) 492 nm  $\times$  250 nm, and (green) 185 nm  $\times$  185 nm. (f) Resonance position as a function of nanoantenna length for simulated (black) and experimental (red) Au NC-based nanoantenna arrays in comparison to experimental resonances for bulk Au (blue) nanoantenna arrays. (g) Normalized transmittance at resonance as a function of the angle of linearly polarized incident light for the nanoantenna arrays shown in a–d.

characterized by spectroscopic ellipsometry and used in the simulations (Supporting Information, Figure S5). Experimental transmittance spectra of these four samples are collected by Fourier transform infrared (FT-IR) spectroscopy (Figure 2e, middle panel). As the nanoantenna length increases from 178 to 863 nm, the measured resonance wavelength shifts from 962 to 3010 nm, closely matching the simulations. For comparison, bulk gold nanoantenna arrays of similar dimensions are fabricated by electron-beam lithography and thermal evaporation of Au. Their transmittance spectra (Figure 2e, bottom panel) show resonances varying from 816 to 2818 nm. Figure 2f plots all the resonance positions as a function of nanoantenna length from simulations and from fabricated Au NC-based and bulk Au nanoantenna arrays. The optical properties of Au NC-based nanoantennas, like bulk Au nanoantennas, red-shift with increasing nanorod length. However, for the same nanorod length, the resonance of Au NC-based nanoantennas are 150–190 nm red-shifted and broader compared with those for bulk Au nanoantennas, which arises from the different permittivity associated with the NC-based metal compared to the bulk material.<sup>33</sup>

Since we fabricate anisotropic nanostructures as building blocks for metasurfaces, we probe their polarization control of incident light. The polarization-dependent transmittance spectra for the four samples in Figure 2a–d are shown as a function of the angle of linearly polarized incident light in Supporting Information, Figure S6. The polarization angle is defined as the angle between the polarization direction and the longitudinal direction of the nanorods (as defined in the inset in Figure 2a). For the anisotropic nanorods (in Figure 2a–c), the magnitude of the transmittance at resonance increases and ultimately reaches approximately 100% as the polarization angle of the incident light is rotated from 0 to 90° (Figure 2g, black, red, and blue symbols). As expected, there is no polarization dependence (Figure 2g, green symbol) for the isotropic 178 nm nanopillars (Figure 2d). The magnitude of the polarization sensitivity increases as the aspect ratio of the nanorods is

increased. For example, the normalized transmittance varies from 0 for isotropic nanostructures (d), to 25% for (c), 60% for (b), and 80% for (a) as the aspect ratio of the nanorods increases. This is consistent with the response of similar size nanorods made of bulk Au (Supporting Information, Figure S7), for which the normalized transmittance increases from 0 to 30%, 70%, and 90% with increasing aspect ratio. We note that, unlike bulk Au nanorods that must be fabricated using a metal adhesion layer, known to deleteriously affect the optical properties,<sup>44,45</sup> NC-based nanorods are advantageously fabricated with  $\sim 90\%$  yield without an adhesion layer. Functionalizing the substrate surface with a self-assembled monolayer may provide a route to reduce even further the defect density and increase the polarization conversion efficiency in Au NC-based nanorods.

Since Au NC-based nanoantennas can control the polarization of light as do their bulk Au analogs, we exploit Au NC-based nanoantennas as building blocks of achromatic QWPs (Figure 3a) that operate at normal incidence in the near-to-mid-infrared region of the electromagnetic spectrum. To do so, we combine arrays of two different length Au NC-based nanorods and interleave them in an orthogonal fashion on a single substrate.<sup>21</sup> The QWP functionality is achieved as the nanorods along the two orthogonal directions mainly interact with the incident polarization along their longitudinal axis, thus realizing a localized birefringence. The phase difference between the 0 and 90° polarized transmitted waves is tailored to be 90° at the desired wavelength range of operation by controlling the length and thickness of the nanorods as well as the gap between them.

The first configuration we implemented is a metasurface QWP designed to operate in the mid-IR (Figure 3a). The length ( $l_i$ ), width ( $w_i$ ), and period ( $d_i$ ) of the nanorods oriented in the  $i$ -x- and  $y$ -directions are  $l_x = 800$  nm,  $w_x = 200$  nm, and  $d_x = 1400$  nm and  $l_y = 1000$  nm,  $w_y = 200$  nm, and  $d_y = 1200$  nm. All nanorods are 150 nm thick, and the gaps between nanorods are 200 nm. Full-wave numerical simulations of the



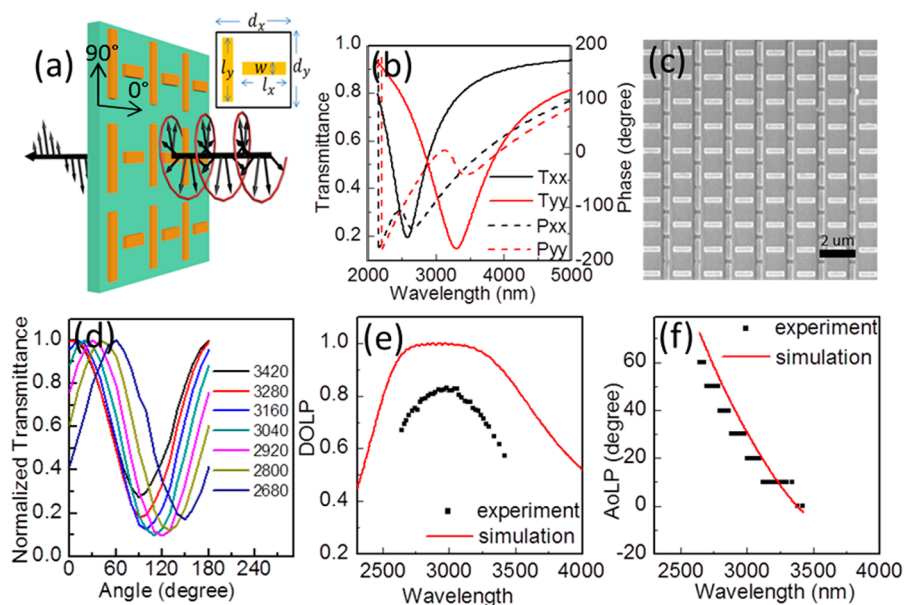


**Figure 3.** (a) Schematic of the design and optical characterization of a metasurface QWP constructed from an orthogonal array of two different size nanorods with length ( $l_i$ ), width ( $w_i$ ), and period ( $d_i$ ) in the  $i = x$ - and  $y$ -directions. (b) Full wave simulations of the transmittance (solid curve) and phase (dashed curve) for the QWP upon excitation by light linearly polarized at 0 and 90°, along the longitudinal axes of the  $x$ -oriented nanorods (black) with  $l_x = 800$  nm,  $w_x = 200$  nm, and  $d_x = 1400$  nm and the  $y$ -oriented nanorods (red) with  $l_y = 1000$  nm,  $w_y = 200$  nm, and  $d_y = 1200$  nm. The nanorod thickness is 150 nm; all gaps between nanorods are 200 nm. (c) SEM image of a nanoimprinted, colloidal Au NC-based orthogonal nanorod array fabricated on a glass substrate. (d) Normalized transmitted light intensity as a function of the angle of the second polarizer for different wavelengths of circularly polarized input light. (e) Degree of linear polarization (DoLP) and (f) angle of linear polarization (AoLP) for circularly polarized input light: simulation (red curve) and experiment result (black dots). The AoLP is collected at a minimum step of 10°.

transmittance spectra and phase for linearly polarized light at 0° (along  $x$ -oriented nanorods) and at 90° (along  $y$ -oriented nanorods), are shown in Figure 3b. The corresponding experimental transmittance spectra are shown in Supporting Information, Figure S8. Simulations show a phase difference close to 90° between the transmitted polarizations (black and red dashed curves in Figure 3b), in a wavelength range spanning 2729–3094 nm. Within this bandwidth of operation, the ratio of transmittance amplitudes for 0 and 90° polarization varies, suggesting that the effective fast and slow axes of this QWP rotate as the wavelength changes. Therefore, for incident circularly polarized excitation, the transmitted light will be linearly polarized, but with a polarization angle that depends on the wavelength.

To fabricate this mid-IR QWP metasurface by nanoimprinting NC-based nanostructures, we design a master template with orthogonal arrays of interleaved nanorods whose dimensions are  $l_x = 970$  nm,  $w_x = 250$  nm, and  $d_x = 1400$  nm and  $l_y = 1130$  nm,  $w_y = 270$  nm, and  $d_y = 1200$  nm. As described above, we deposit the Au NCs by spin-coating, then lift off the imprint resist in acetone, and immerse the patterned NC thin film in an acetone solution of SCN. The dimensions of the template are designed to be larger than those of the desired final structures to compensate for shrinkage of the NC-based nanostructures upon ligand exchange. We fabricate the metasurface QWP over a 1.2 mm × 1.2 mm area on a glass substrate. Figure 3c shows a SEM image of a nanoimprinted NC-based QWP. Larger-area and higher resolution images of the QWP are shown in Supporting Information, Figure S9 and Figure S10. The dimensions of the fabricated nanorods are measured from SEM images taken from nine different areas of this QWP. The average dimensions of the nanorods are  $l_x = 821$  nm,  $w_x = 241$  nm, and  $d_x = 1400$  nm and  $l_y = 964$  nm,  $w_y =$

261 nm, and  $d_y = 1200$  nm. Across the large area of the QWP the variations in the dimensions are within 2–6%. For nanorods oriented in the  $x$ - and  $y$ -direction of the QWP, the LER is 2.9 nm, and the misalignment is 0.2° (Supporting Information, Table 1). The height of the nanorods is 109 nm, thinner than that in the design, but within tolerance to allow the successful operation and high polarization conversion efficiency of the QWP.

To characterize the optical properties of the Au NC-based QWP, we excite the sample with monochromatic, circularly polarized light generated by passing light from an FT-IR spectrometer through a linear polarizer and then a commercial mid-IR (2800 nm) QWP. A second linear polarizer is placed between the sample and the detector and rotated from 0 to 180 deg in steps of 10 degrees to analyze the angular-dependence of the transmitted light at each wavelength. Figure 3d shows the normalized transmittance as a function of the angle of the second polarizer. The sinusoidal shape of the angular-dependence of the transmitted light suggests that the output light is linearly polarized to a large degree. The troughs in the sinusoid should be ideally zero, however nonidealities in the dimensions of the nanorod arrays from the designed structure and the less than perfect polarization ability of the commercial mid-IR QWP likely give rise to residual transmittance.

We extract the degree of linear polarization (DoLP) from the measured NC-based QWP optical properties shown in Figure 3d. The DoLP is defined as  $I(\lambda)_{\max} - I(\lambda)_{\min} / I(\lambda)_{\max} + I(\lambda)_{\min}$ , where  $I(\lambda)_{\max}$  and  $I(\lambda)_{\min}$  are the maximum and minimum in the transmitted light intensity at specific polarization angles for a given wavelength  $\lambda$ . The wavelength-dependent DoLP for the circularly polarized light incident on the fabricated QWP is shown in Figure 3e (black dots). The measurements are in good agreement with simulations of the DoLP for the designed

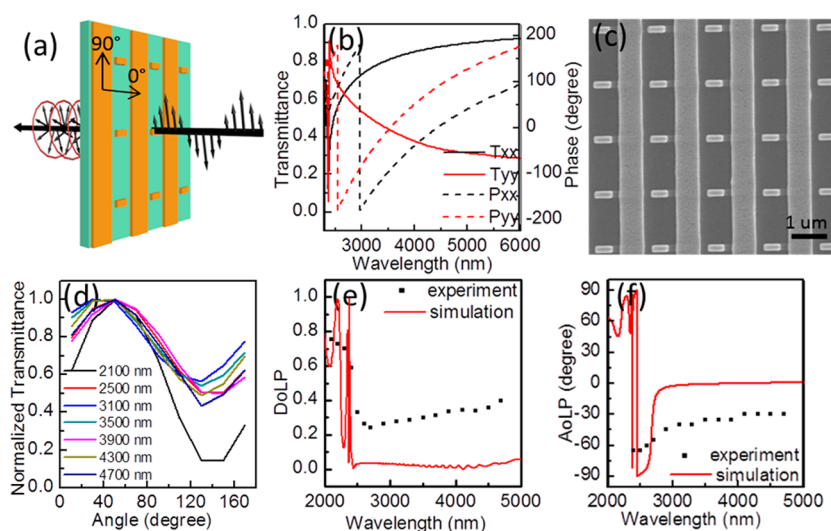


**Figure 4.** (a) Schematic of the design and optical characterization of an extreme bandwidth, metasurface QWP constructed from a short nanorod, and a continuous line. (b) Full wave simulations of the transmittance (solid curve) and phase (dashed curve) for the extreme bandwidth, QWP upon excitation by light linearly polarized at 0 and 90°, along the longitudinal axes of the short,  $x$ -oriented nanorod (black) with  $l_x = 500$  nm,  $w_x = 200$  nm, and  $d_x = 1600$  nm and the  $y$ -oriented nanoline (red) with  $w_y = 700$  nm. The thickness is 150 nm; all gaps between  $x$ -oriented nanorod and  $y$ -oriented nanoline are 200 nm. (c) SEM image of a nanoimprinted, colloidal Au NC-based extreme bandwidth QWP on glass substrate. (d) Normalized transmitted light as a function of the angle of the second polarizer for different wavelengths of linearly polarized input light. (e) Degree of linear polarization (DoLP) and (f) angle of linear polarization (AoLP) for linearly polarized input light: simulation (red curve) and experiment (black dots).

plate (red curve). The DoLP of the NC-based QWP is sufficiently large ( $>0.8$ ) over a wavelength range of 2840–3080 nm, which is comparable to that of previously reported QWPs fabricated by electron-beam lithography and metal evaporation.<sup>21</sup> The angle of linear polarization (AoLP) is defined as the polarization angle of the transmitted linearly polarized light for this mid-IR QWP. The wavelength-dependence of the AoLP is extracted from Figure 3d and plotted in Figure 3f (black dots). The experimental AoLP is clustered in lines, limited by the resolution with which we collected the output angle, but closely matches the simulation (red curve).

To broaden the operational wavelength range of the QWP, an extreme bandwidth design is explored (Figure 4a), in which vertically oriented nanorods are extended to form a continuous line with a width of 700 nm, while the horizontally oriented nanorods are reduced to 500 nm in length.<sup>21,38</sup> The continuous, vertical line effectively moves the nanorod resonance into the far-IR, thus eliminating unwanted phase dispersion from the vertical nanorods in the mid-IR.<sup>21</sup> The short horizontal nanorods introduce phase dispersion in the near-IR and a constant 90° difference with respect to the vertically oriented line at lower wavelengths in the near-to-mid infrared, as shown in Figure 4b. Without the horizontal nanorods the continuous, vertical metal lines would create a linear polarizer. The ratio of the transmittances for light polarized along the  $y$ -oriented nanolines to that for light polarized along the  $x$ -oriented nanorods vary from 1.5 to 0.5, and reaches 1 at 2700 nm, which implies that the effective optical axes overlap at this wavelength. Using the same fabrication methods described above, we fabricate the extreme bandwidth QWP by nanoimprinting of colloidal Au NCs on a glass substrate. Figure 4c and Supporting Information Figure S11 show SEM images of the fabricated waveplate. The dimensions of the nanorods oriented in the  $x$ -direction are  $l_x = 469$  nm;  $w_x = 178$  nm, and  $d_x = 1600$  nm and of the nanoline in the  $y$ -direction are  $w_y = 641$ . The gap between nanorods is 245 nm, and their thickness is 80 nm. The

LER and misalignment are 4.5 nm and 0.6° for the  $x$ -oriented nanorods and are 7 nm and 0.1° for the  $y$ -oriented nanolines (Supporting Information, Table 1). This is the first experimental realization of an extreme bandwidth metasurface QWP based on our orthogonal nanorod design.

To characterize the mid-IR waveplate in Figure 3, we generate circularly polarized light using a commercial QWP and analyze the linearly polarized transmitted light through our sample. However, there are no available commercial mid-IR QWPs that have the extreme bandwidths realized by our design in Figure 4 to provide circularly polarized incident light. Therefore, in order to characterize the optical properties of the extreme bandwidth QWP, we excite the sample with light linearly polarized along angles varying from 0 to 90° in steps of 5°. This is achieved by placing and rotating a broadband linear polarizer between the source and the sample. A second linear polarizer is positioned behind the sample and before the detector to record the angular-dependence of the amplitude of the transmitted light. In theory, if linearly polarized incident light has the same components on the effective fast and slow axes of the sample, the transmitted light will be circularly polarized. Since we do not know where the effective fast and slow axes are for each wavelength, we test all possible angles for the incident light, and then pick out the transmitted light with the smallest DoLP at each wavelength. The intensity of transmitted light with the smallest DoLP at different wavelengths is plotted in Figure 4d as a function of the angle of the second polarizer. The DoLP for these spectra are plotted in Figure 4e (black dots). There is an extreme, broad wavelength range (2500–4700 nm) over which the DoLP is remarkably small. This working wavelength range agrees well with the full-wave simulation (red curve) where a near zero DoLP starts at 2500 nm and extends to 5000 nm. The difference in the DoLPs between experiment and simulation likely arises from variations in the nanorod dimensions. For the extreme bandwidth QWP, the corresponding AoLP is defined as the angle of the first

polarizer for which the DoLP is minimum (Figure 4f). Simulations (red curve) and experiments (black dots) agree well and highlight the expected dispersion of the fast and slow axes over the bandwidth of operation for this extreme bandwidth QWP.

In summary, we have demonstrated a fast, large-area, solution-based fabrication method for size-tunable nano-crystal-based nanoantennas and exploited their plasmonic resonance and their polarization sensitivity to fabricate ultrathin metasurfaces that operate as near-to-mid infrared QWPs. The fabrication of Au NC-based plasmonic nanostructures provides a promising route to scalable manufacturing of more complex, optical metamaterial devices, such as plasmonic biosensors, meta-lenses, holography plates, and optical nanocircuits.

## ■ ASSOCIATED CONTENT

### Supporting Information

Methods for NC synthesis, nanoimprint lithography and optical measurements. Additional SEM images of a master template, nanoantenna arrays, and metasurface quarter-wave plates. AFM images for nanoantenna arrays. Ellipsometry measurement data for SCN-exchanged Au NC thin film. Polarization-dependent transmittance spectra for nanoantenna arrays. Transmittance spectra for metasurface quarter-wave plate. The Supporting Information is available free of charge on the ACS Publications website at DOI: 10.1021/acs.nanolett.5b02647.

## ■ AUTHOR INFORMATION

### Corresponding Author

\*E-mail: kagan@seas.upenn.edu. Phone: (215) 573-4384. Fax: (215) 573-2068.

### Notes

The authors declare no competing financial interest.

## ■ ACKNOWLEDGMENTS

We thank Dr. Sung-Hoon Hong for his help with nanoimprint lithography and Dr. Soong Ju Oh for his help with electron-beam lithography. We thank Ethan Glor and Tianyi Liu for their help with ellipsometry measurements. The authors are grateful for primary support of this work from the Office of Naval Research Multidisciplinary University Research Initiative Award No. ONR-N00014-10-1-0942. Scanning electron microscopy was performed in facilities supported by the NSF MRSEC Program under Award No. DMR05-1120901.

## ■ REFERENCES

- (1) Soukoulis, C. M.; Wegener, M. *Nat. Photonics* **2011**, *5*, 523–530.
- (2) Shalaev, V. M. *Nat. Photonics* **2007**, *1*, 41–48.
- (3) Zheludev, N. I.; Kivshar, Y. S. *Nat. Mater.* **2012**, *11*, 917–924.
- (4) Haug, F. J.; Söderström, T.; Cubero, O.; Terrazzoni-Daudrix, V.; Ballif, C. *J. Appl. Phys.* **2008**, *104*, 064509.
- (5) Shen, H.; Bienstman, P.; Maes, B. *J. Appl. Phys.* **2009**, *106*, 073109.
- (6) Le, F.; Brandl, D. W.; Urzhumov, Y. A.; Wang, H.; Kundu, J.; Halas, N. J.; Aizpurua, J.; Nordlander, P. *ACS Nano* **2008**, *2*, 707–718.
- (7) Adato, R.; Yanik, A. A.; Amsden, J. J.; Kaplan, D. L.; Omenetto, F. G.; Hong, M. K.; Erramilli, S.; Altug, H. *Proc. Natl. Acad. Sci. U. S. A.* **2009**, *106*, 19227–19232.
- (8) Bakker, R. M.; Yuan, H. K.; Liu, Z.; Drachev, V. P.; Kildishev, A. V.; Shalaev, V. M.; Pedersen, R. H.; Gresillon, S.; Boltasseva, A. *Appl. Phys. Lett.* **2008**, *92*, 043101.
- (9) Zhang, Y.; Aslan, K.; Previte, M. J. R.; Malyn, S. N.; Geddes, C. D. *J. Phys. Chem. B* **2006**, *110*, 25108–25114.
- (10) Saboktakin, M.; Ye, X.; Chettiar, U. K.; Engheta, N.; Murray, C. B.; Kagan, C. R. *ACS Nano* **2013**, *7*, 7186–7192.
- (11) Li, J.; Fattal, D.; Li, Z. *Appl. Phys. Lett.* **2009**, *94*, 263114.
- (12) Shen, C.; Hui, C.; Yang, T.; Xiao, C.; Tian, J.; Bao, L.; Chen, S.; Ding, H.; Gao, H. *Chem. Mater.* **2008**, *20*, 6939–6944.
- (13) Stewart, M. E.; Anderton, C. R.; Thompson, L. B.; Maria, J.; Gray, S. K.; Rogers, J. A.; Nuzzo, R. G. *Chem. Rev.* **2008**, *108*, 494–521.
- (14) Lu, H.; Liu, X.; Mao, D.; Wang, G. *Opt. Lett.* **2012**, *37*, 3780–3782.
- (15) Knight, M. W.; Sobhani, H.; Nordlander, P.; Halas, N. J. *Science* **2011**, *332*, 702–704.
- (16) Atwater, H. A.; Polman, A. *Nat. Mater.* **2010**, *9*, 205–213.
- (17) Bai, W.; Gan, Q.; Song, G.; Chen, L.; Kafafi, Z.; Bartoli, F. *Opt. Express* **2010**, *18*, A620–A630.
- (18) Ni, X.; Ishii, S.; Kildishev, A. V.; Shalaev, V. M. *Light: Sci. Appl.* **2013**, *2*, e72.
- (19) Chen, X.; Huang, L.; Mühlenbernd, H.; Li, G.; Bai, B.; Tan, Q.; Jin, G.; Qiu, C.-W.; Zhang, S.; Zentgraf, T. *Nat. Commun.* **2012**, *3*, 1198.
- (20) Aieta, F.; Genevet, P.; Kats, M. A.; Yu, N.; Blanchard, R.; Gaburro, Z.; Capasso, F. *Nano Lett.* **2012**, *12*, 4932–4936.
- (21) Zhao, Y.; Alù, A. *Nano Lett.* **2013**, *13*, 1086–1091.
- (22) Yu, N.; Aieta, F.; Genevet, P.; Kats, M. A.; Gaburro, Z.; Capasso, F. *Nano Lett.* **2012**, *12*, 6328–6333.
- (23) Ellenbogen, T.; Seo, K.; Crozier, K. B. *Nano Lett.* **2012**, *12*, 1026–1031.
- (24) Jiang, Z. H.; Lin, L.; Ma, D.; Yun, S.; Werner, D. H.; Liu, Z.; Mayer, T. S. *Sci. Rep.* **2014**, *4*, 7511.
- (25) Yu, N.; Genevet, P.; Kats, M. A.; Aieta, F.; Tetienne, J.-P.; Capasso, F.; Gaburro, Z. *Science* **2011**, *334*, 333–337.
- (26) Huang, L.; Chen, X.; Mühlenbernd, H.; Li, G.; Bai, B.; Tan, Q.; Jin, G.; Zentgraf, T.; Zhang, S. *Nano Lett.* **2012**, *12*, 5750–5755.
- (27) Huang, L.; Chen, X.; Mühlenbernd, H.; Zhang, H.; Chen, S.; Bai, B.; Tan, Q.; Jin, G.; Cheah, K.-W.; Qiu, C.-W.; Li, J.; Zentgraf, T.; Zhang, S. *Nat. Commun.* **2013**, *4*, 2808.
- (28) Ni, X.; Kildishev, A. V.; Shalaev, V. M. *Nat. Commun.* **2013**, *4*, 2807.
- (29) Chou, S. Y.; Krauss, P. R.; Renstrom, P. J. *Science* **1996**, *272*, 85–87.
- (30) Boltasseva, A. *J. Opt. A: Pure Appl. Opt.* **2009**, *11*, 114001.
- (31) Lucas, B. D.; Kim, J.-S.; Chin, C.; Guo, L. J. *Adv. Mater.* **2008**, *20*, 1129–1134.
- (32) Henzie, J.; Lee, M. H.; Odom, T. W. *Nat. Nanotechnol.* **2007**, *2*, 549–554.
- (33) Fafarman, A. T.; Hong, S. H.; Caglayan, H.; Ye, X.; Diroll, B. T.; Paik, T.; Engheta, N.; Murray, C. B.; Kagan, C. R. *Nano Lett.* **2013**, *13*, 350–357.
- (34) Fafarman, A. T.; Hong, S. H.; Oh, S. J.; Caglayan, H.; Ye, X.; Diroll, B. T.; Engheta, N.; Murray, C. B.; Kagan, C. R. *ACS Nano* **2014**, *8*, 2746–2754.
- (35) Ahn, S. H.; Guo, L. J. *Adv. Mater.* **2008**, *20*, 2044–2049.
- (36) Liang, C.-C.; Liao, M.-Y.; Chen, W.-Y.; Cheng, T.-C.; Chang, W.-H.; Lin, C.-H. *Opt. Express* **2011**, *19*, 4768–4776.
- (37) You, E. A.; Zhou, W.; Suh, J. Y.; Huntington, M. D.; Odom, T. W. *ACS Nano* **2012**, *6*, 1786–1794.
- (38) Zhao, Y.; Alù, A. *Phys. Rev. B: Condens. Matter Mater. Phys.* **2011**, *84*, 205428.
- (39) Peng, S.; Lee, Y.; Wang, C.; Yin, H.; Dai, S.; Sun, S. *Nano Res.* **2008**, *1*, 229–234.
- (40) Jung, G. Y.; Wu, W.; Ganapathiappan, S.; Ohlberg, D. A. A.; Saif Islam, M.; Li, X.; Olynick, D. L.; Lee, H.; Chen, Y.; Wang, S. Y.; Tong, W. M.; Williams, R. S. *Appl. Phys. A: Mater. Sci. Process.* **2005**, *81*, 1331–1335.
- (41) Ko, S. H.; Park, I.; Pan, H.; Grigoropoulos, C. P.; Pisano, A. P.; Luscombe, C. K.; Fréchet, J. M. J. *Nano Lett.* **2007**, *7*, 1869–1877.
- (42) Maier, S. A. *Plasmonics: Fundamentals and Applications*, 1st ed.; Springer: New York, 2007.
- (43) Alù, A.; Engheta, N. *Phys. Rev. Lett.* **2008**, *101*, 043901.

- (44) Habteyes, T. G.; Dhuey, S.; Wood, E.; Gargas, D.; Cabrini, S.; Schuck, P. J.; Alivisatos, A. P.; Leone, S. R. *ACS Nano* **2012**, *6*, 5702–5709.
- (45) Zhao, Y.; Belkin, M. A.; Alù, A. *Nat. Commun.* **2012**, *3*, 870.